Egypt. J. Chem. **Vol. 68**, No. 3. pp. 493 - 510 (2025)

Egyptian Journal of Chemistry

http://ejchem.journals.ekb.eg/

Transition Metal Tungstate's Electrocatalyst Supported on a Mixture of Reduced Graphene Oxide and Silica Template for Water Splitting

R. S. Amin[a], Amani E. Fetohi[a], Dena Z. Khater[a], K. M. El-Khatib[a,*]

[a] *Chemical Engineering Department, Engineering Research and Renewable Energy Institute, National Research Centre, 33 El-Buhouth St., Dokki, Cairo, 12622, Egypt*

Abstract

Developing efficient and cost-effective electrocatalysts for water splitting in an alkaline medium is critical. A series of nano-structured metal tungstate MWO_4 (M = Co, Ni, Mn, Zn, and Fe) is anchored on a reduced graphene oxide and silica template via a one-pot hydrothermal method. The electrochemical performance of the electrocatalysts is evaluated for hydrogen and oxygen evolution reactions. All the electrocatalysts show good performance in both reactions. $MnWO_4$/rGO-ST/NF is the most efficient electrocatalyst for HER, at current densities of 10 and 50 mA cm^{-2}, it requires overpotential values of 150 and 232 mV, respectively (Tafel slope 130 mV dec^{-1}). In the case of OER, $Fe_2(WO_4)_3$/rGO-ST/NF has the best performance with over potential values of 322, 339, and 352 mV at 10, 30, and 50 mA cm^{-2} respectively (Tafel slope 44 mV dec^{-1}). $MnWO_4$/rGO-ST/NF||$Fe_2(WO_4)_3$/rGO-ST/NF electrode pair exhibits exceptional 12-hour durability and cell voltage of 1.81 V for water splitting.

Keywords: Transition Metal tungstate's, reduced graphene oxide, silica template, Hydrogen, and Oxygen evolution reaction, water splitting

1. Introduction

The rising worldwide energy use and the associated environmental damage imposed on the scientific community's development of clean and long-lasting energy systems [1]. Hydrogen has long been regarded as the perfect sustainable energy source due to its special characteristics such as high conversion efficiency, low pollution, and high energy density [2–4]. Nowadays, mosthydrogen manufacturing processes produce a substantial quantity of carbon dioxide, producing serious environmental difficulties [5, 6]. Electrochemical water splitting is another sustainable energy method lately used for hydrogen production and to meet the expanding energy demands [7]. This process involves two reactions, hydrogen evolution reaction (HER) which takes place at the cathode and includes the recombination of protons and electrons, and the other reaction is oxygen evolution reaction (OER) at the anode which includes water splitting into oxygen gas and protons.The demand of voltage for the electrochemical water splitting is 1.23 V but in case of the industrial applications this value is increased above 1.8 V to overcome the energy barriers. Noble metals-based electrocatalysts such as Pt, Ir, and Ru have been used to allow the water-splitting reaction at reduced values of potential. Still, these kinds of electrocatalysts are expensive and rare. Hence, it is very essential to develop different kinds of electrocatalysts that depend mainly on transition metals and transition metal oxides to expand in industrial applications [8]. Tungsten oxide is thought to be one of the most desirable electrocatalyst materials due to its chemical stability, environmental friendliness, and adaptable composition and structure [9].

However, tungsten oxide has low conductivity and a restricted number of active sites. So, to improve its electrochemical performance toward water splitting reactions, by anchoring tungsten oxide with transition metal oxides [10, 11], and carbon-based materials such as graphene, carbon nanotubes, and reduced graphene oxide [12–14].Mesoporous structures are characterized by having a large specific surface area and pores with diameters between 2 and 50 nm. Among inorganic structures, mesoporous silica spheres found wide applications especially in catalysis because of their internalcavity and enhanced surface-to-volume ratio. The higher surface area provides the catalysts with more chances to reach target molecules and increase catalytic activity. Moreover, the silica template is easy to synthesizewhich enhances the availability for mass production [15-17].From another point of view, nickel foam (NF), as a result of its high porosity, is commonly utilized as a catalyst carrier, providing a greater area for catalytic development and maximizing electrolyte contact [18].

*Corresponding author e-mail: kamleced@hotmail.com.; (K.M. El-Khatib).
Received date 27 June 2024; Revised date 30 July 2024; Accepted date 07 August 2024
DOI: 10.21608/EJCHEM.2024.299575.9911

Because of their customizable electronic structure, comparatively low toxicity, controllable microstructure, environmental friendliness, and abundance of resources, metal tungstate's have sparked widespread concern when compared to numerous transition metal oxides, Furthermore, due to their intrinsic high conductivity and the diverse oxidation states of W, metal tungstate's outperform metal oxides in electrocatalytic performance [19,20].

As a result, metal tungstate's are thought to have superior electrocatalytic performance in the realm of electrochemistry [21]. Xin Yue et al. [22]prepared $Ni_{0.19}WO_4$ nanowires supported on Ni foam prepared by hydrothermal and heating process and applied for water splitting in an alkaline medium, the findings showed that the overpotential values for HER and OER at 10 mA cm^{-2} are 200 mV and 260 mV, respectively.

An overpotential of 310 mV is acquired at 10 mA cm^{-2} in the as-grown $NiCo_2O_4$@$NiWO_4$ core-shell nanorod arrays investigated for the oxygen evolution process in an alkaline solution [23]. Again, hydrothermal synthesis and annealing treatment are used to prepare WO_2 hexahedral networks supported on nickel foam, they found that, at 10 mA cm^{-2}, an overpotential value of 48 mV for the HER and that of 300 mV for the OER in an alkaline solution [24].The performance of hierarchical WO_3 with nanowires on a nanosheet array toward OER in an alkaline medium has been studied by JinxiangDiao et al. [25] they stated that the electronic structure of WO_3 with oxygen vacancies corresponds perfectly with the requirements of OER; the electrocatalyst achieved 0.23 V overpotential at 10 mA cm^{-2}.Additionally, the oxygen vacancies and Fe_2P&$WO_{2.92}$ synergy were crucial to the Fe_2P-$WO_{2.92}$/NF's strong electrochemical performance towards OER in an alkaline media because they provided effective active sites for the reaction. At 100 mA cm^{-2}, the electrocatalyst exhibits a low overpotential of 267 mV [26]. Mesoporous WO_3-TiO_2 was prepared by an acid-catalyzedpeptization method and tested for alkaline (HER). Its exchange current density is 6.2 x 10^{-5} mA cm^{-2}, and its low overpotential value is 120 mV. [27].

In this study, we prepare bi-functional electrocatalysts based on metal tungstate nanoparticles (M = Co, Ni, Mn, Zn, and Fe) supported on a mixture of reduced graphene oxide (rGO) and silica template(ST) using a one-pot hydrothermal method. The following electrocatalysts prepared are namely: Cobalt tungstate ($CoWO_4$/rGO-ST), Nickel tungstate $NiWO_4$/rGO-ST, Manganese tungstate $MnWO_4$/rGO-ST, Zinc tungstate $ZnWO_4$/rGO-ST, and Iron (III) tungstate $Fe_2(WO_4)_3$/rGO-ST. The total loading of the electrocatalysts on the support is set at 30%, and the atomic ratio of tungsten to the transition metals is determined to be 1:1. To the best of our knowledge, these novel constructions of prepared electrocatalysts have been rarely tested for water splitting in an alkaline medium.

2. Materials and Methods

Materials

All chemical is purchased from Sigma-Aldrich (USA) in analytical grade, and it is used without being purified. Double-distilled water is used to make all aqueous solutions, including cleaning and preparation.

Preparation of transition metal tungstate's supported on a mixture of rGO and ST

The synthesis of mixed support materials rGO and silica template was mentioned previously [28]. **Scheme 1** illustrates the one-pot hydrothermal method used to prepare the electrocatalysts. Tungsten and transition metals (Co, Zn, Mn, Ni, and Fe) are supported on a combination of rGO and ST. The total loading of the electrocatalysts on the support was fixed at 30 %. Generally, calculated amounts of sodium tungstate dihydrate ($Na_2WO_4.2H_2O$) and transition metal chlorides are added to 50 ml of double-distilled water, and then the pH of the solution is adjusted to 3 by adding 1 molar HCl solution. The measured amount of support (rGO and ST) was added to the mixture followed by hydrothermal treatment in the autoclave at 180 ^{0}C for 12 h. The products were filtered, repeatedly cleaned with double-distilled water once they had cooled to room temperature, and vacuum-dried for six hours at 60 °C. The electrocatalysts that were prepared in accordance with the above-mentioned procedure were specifically as follows: Cobalt tungstate ($CoWO_4$/rGO-ST), Nickel tungstate $NiWO_4$/rGO-ST, Manganese tungstate $MnWO_4$/rGO-ST, Zinc tungstate $ZnWO_4$/rGO-ST, and Iron (III) tungstate $Fe_2(WO_4)_3$/rGO-ST.

Physical characterization of the electrocatalysts

An X-ray diffraction (XRD) system, such as the Rigaku-D/MAX-PC 2500, is used to analyse the crystalline phase. Microstructure and morphology are examined using high-resolution transmission electron microscopy (HRTEM, JEOL-JEM 2010) and scanning electron microscopy (SEM). The electrocatalyst's valence states are identified via X-ray photoelectron spectroscopy (XPS) (PH1-5700 ESCA system, US).

Electrochemical characterization

Electrode preparation

To prepare the catalyst slurry, the catalyst and polyvinylidene fluoride (PVDF) are mixed with a ratio of 9:1 by weight in N-Methyl-2-Pyrrolidone (NMP) solvent. The combination is then subjected to sonication for more than an hour, resulting in a homogeneous dispersion of the slurry. Nickel foam with 1 cm^2 cleaned with sonication in HCl (3 M), ethanol, and deionized water for 15 min. each, is dried in a vacuum oven at 60 °C for eight hours. The slurry is drop cast on 1cm^2 nickel foam to make a working electrode (the loading mass is about 1.0 mg cm^{-2}) for electrochemical evaluation.

Electrochemical characterization of Electrocatalyst

A three-electrode setup with a Voltalab 6 electrochemical workstation is used to assess the electrocatalytic activity. The platinum wire serves as the counter electrode, while an Ag/AgCl electrode that has been saturated with KCl serves as the reference electrode. HER and OER polarization curves are obtained by linear sweep voltammetry (LSV) in 1.0 M KOH with a scan rate of 5 mV s^{-1} and corrected with iR compensation. In the turnover zone of the HER and OER, electrochemical impedance spectroscopy (EIS) evaluation is carried out in the range of frequency 0.1-10^5 Hz with a polarized potential. The Nernst equation is used to convert all potentials to the reversible hydrogen electrode (RHE): E_{RHE} = E(Ag/AgCl) + 0.197 + 0.059 pH. The electrochemical double-layer capacitance (Cdl), which may be estimated from CV curves, is used to determine the electrochemically active surface areas (ECSA) of electrocatalysts as obtained. Throughout the non-Faradaic potential range, cyclic voltammograms (CV) are captured at increasing scan speeds (40-200 mV s^{-1}).

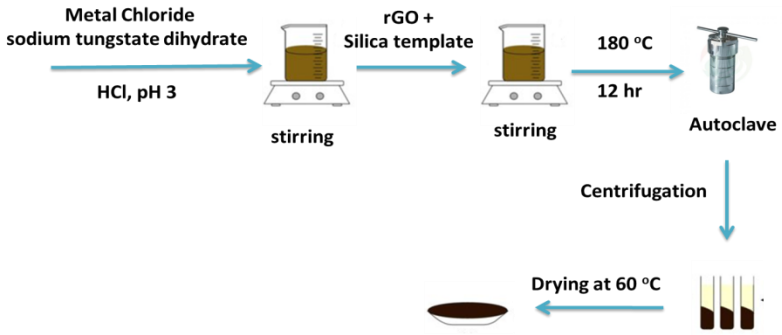

Scheme 1. The procedure of preparation of metal tungstate supported on rGO and ST.

3. Results and Discussion

Physical characterization

The crystal phase composition and purity of the transition metal tungstate's electrocatalysts are investigated. As shown in **Figure 1.**, in all the XRD patterns, the peak around 23~24º could be related to the support (reduced graphene oxide rGO) [29]. It could be noticed that some secondary peaks of transition metal tungstate's have similar positions with the peak of rGO which implies that both the oxides and the support are well stacked with each other. A wider peak is seen for rGO at roughly 23~24º after the oxygen-containing functional groups are mostly removed during the chemical and thermal reduction of GO. This may be clarified as follows: The synthesized rGOs significantly restore the p-conjugated structure of graphene. Because of graphite's high crystallization structure, a wide (002) peak is present in the crystal phase of rGOs, indicating that the layers of rGOs are randomly arranged in accordance with graphite. Generally, the formation of one or more rGO layers following GO reduction may be the cause of the random arrangement. The structure of the graphene nanolayers lies between crystalline and amorphous structures. [30, 31].All the diffraction peaks of metal tungstate's are well indexed to a monoclinic phase furthermore, an amorphous structure is observed for all electrocatalysts. **Figure 1(a)** displays the characteristic peaks at 19.10º, 24.61º, 30.61º, 36.17º, 53.92º and 65.05º are indexed to the (100), (-110), (111), (002), (-202), and (132) diffraction planes of Cobalt tungstate ($CoWO_4$), respectively (PDF 01-072-0479) [32]. Nickel tungstate ($NiWO_4$) XRD graph is illustrated in **Figure 1(b),** it has characteristic peaks at 19.27º, 23.29º, 24.89º, 30.90º, 36.48º, 37.20º, 46.38º, 54.60º and 65.40º are related to the (100),(011), (110), (111), (002), (120), (211), (202) and (222) diffraction plane (PDF15-0755), respectively [33].

The 2θ characteristic peaks of Manganese tungstate ($MnWO_4$) is viewed in **Figure 1(c)** at 15.36º, 18.36º, 23.54º, 24.02º, 29.78º, 31.01º, 35.90º, 37.22º, 40.26º, 40.83º, 44.33º, 48.17º,49.20º, 51.13º,52.29º, 53.01 º,60.54º and 64.33º indexed to the (010), (100), (011), (110), (-111), (020), (002), (200), (-102), (121), (112), (022), (220), (130), (122), (221), (-113) and (132) diffraction plane(PDF 01-085-5966) [34]. While the XRD pattern of Zinc tungstate ($ZnWO_4$) reflected peaks at 2θ values around 15.47º, 18.90º, 23.83º, 24.57º, 30.74º, 31.26º, 36.31º, 38.33º, 44.23º, 45.45º, 47.67º, 52.55º, 62.24º and 64.78º that related to the (010), (100), (011), (110), (111), (020), (021), (200), (112), (211), (030), (122), (-113) and (-311) diffraction plane of $ZnWO_4$ (PDF 73-0554), respectively(**figure (1d)**)[21] . The XRD pattern of iron (iii) tungstate could be referred to the monoclinic phase of $Fe_2(WO_4)_3$ where the diffraction peaks located at 2θ around 22.80º, 25.67º, 27.22º and 30.00º(PDF 00-038-0200) and represented the diffraction planes of (202), (-322), (-224) and (-422) respectively(**figure (1e**)).

The preliminary elemental identification of the $CoWO_4$/rGO-ST, $NiWO_4$/rGO-ST $MnWO_4$/rGO-ST, $ZnWO_4$/rGO-ST and $Fe_2(WO_4)_3$/rGO-ST are performed using XPS and the full-ranged spectra (0-1400 eV) are illustrated in **Figure S1(d)**, correspondingly. It could be distinguished that the existence of C 1s, O 1s, Si 2p, and W 4f, Zn 2p, Fe 2p, and Ni 2p regions at binding energies (BEs) of ~288.048, ~535.634, ~106.206, ~35.516, 1023.69, 738.08 and 858.21 eV,respectively. Furthermore, both Co 2p and Mn 2p for are vanished or difficulty seen, these might be due to the continuation of mixed Mn^{2+}/Mn^{4+} orCo^{2+}/Co^{3+}[35-38]. The high-resolution C1s spectra as illustrated in **Figure S1(a),** deconvoluted into a major peak fitted approximately at 284.246 eV that attributed to the C-C/C=C bonds and accountable for almost 57.926eVAt.% of rGO. Moreover, the incidence of shoulder oxygen-containing groups that could be assigned to C-O (286.29eV, 17.245 At. %), C=O (287.94eV, 10.25 At. %), C-O-C (285.7eV, 21.81 At. %) and O-C=O (290.24 eV, 6.18 At. %). Significantly as indicated in **Figure S1(b)**, the O 1s surface photoemission spectrum identified the presence of three distinct peaks at 530.564, 532.978 and 534.536eV that could be indexed to O^{2-}, OOH^{-}, and $(O^{2-})_3$ ions in the oxide, respectively [39]. The core

level spectra of Si as displayed in **Figure S1(c)** are deconvoluted into two peaks that ascribed to the -C-Si-O (103.79 eV) and O-Si-O bonds (105.58 eV), which indicates that the oxide moves to the stoichiometric SiO_2 [40].

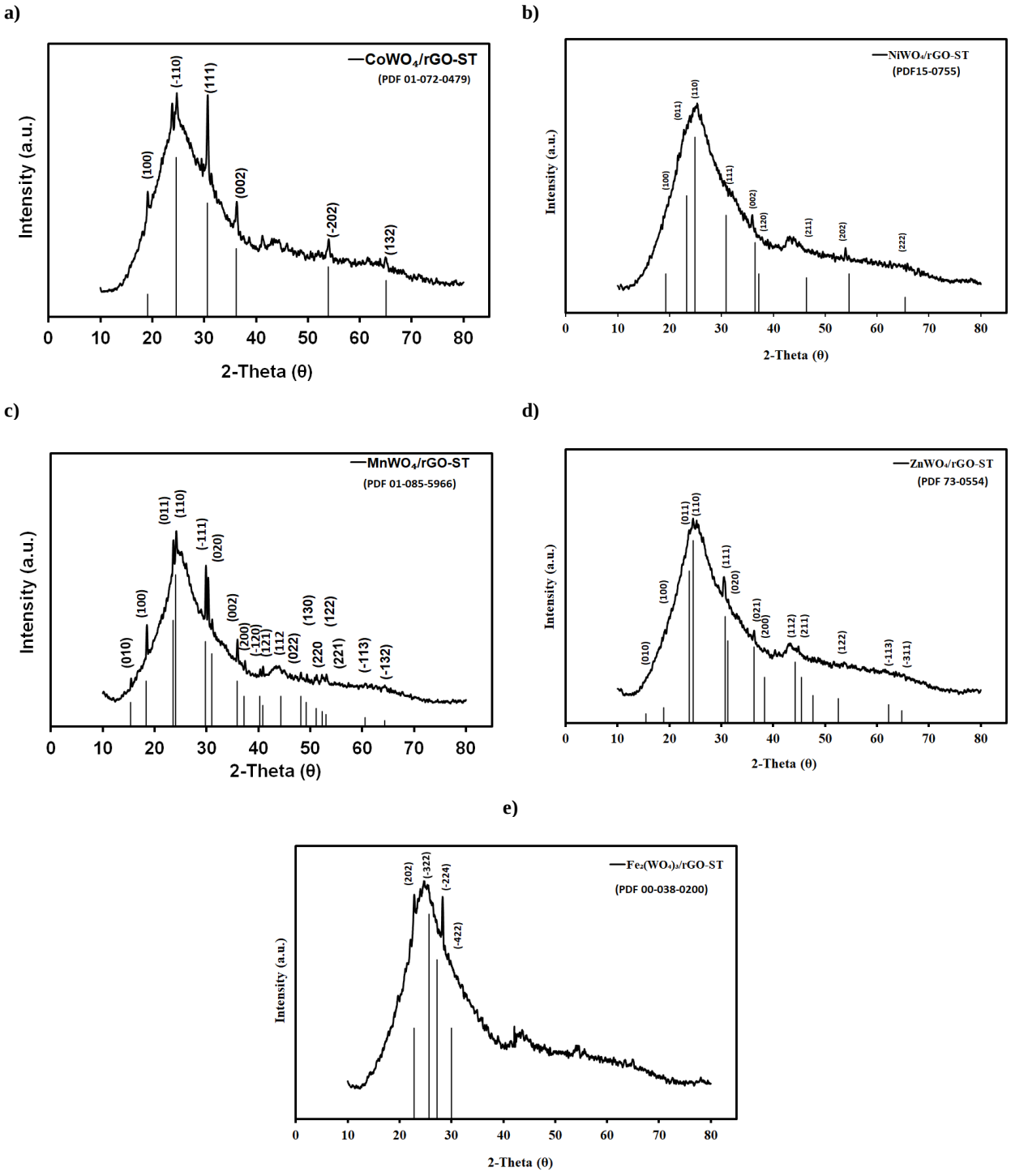

Figure 1: XRD patterns of the support (rGO-ST) and the prepared metal tungstate's M-WO_4/rGO-ST (M = Co, Ni, Mn, Zn & Fe).

As represented in **Figure 2(a-e),** the core-level W4f photoemission spectrum recognized the presence of two distinct doublet peaks for all electrocatalysts at ~35.192 and 37.266 eV that indexed to W 4f $_{7/2}$ and W 4f $_{5/2}$,respectively, which might be attributed to a good extent with W^{6+} [41]. These results are in accordance with the literature [42, 43]. Besides, the presence of an extra shoulder peak at 39.65 eVis related to WO_2 or WO_xin the transition layer that is observed in $Fe_2(WO_4)_3$/rGO-ST [44]. The Co 2p spectrum as displayed in **Figure 2(a')** is fitted as Co $2p_{3/2}$, Co $2p_{1/2,}$ and shake-up satellites. The BEs at 782.56, 785.43, and 796.83 eV are assigned to the formation of Co^{2+} valence. Furthermore, there is a contribution of some Co $^{3+}$ at BE of 779.7 eV with an intensity of 16.95 At. % that is lower than Co^{2+} (60.58 At.%) by 3.4%

[45]. The co-existence of shake-up satellites with strong intensities of 30.96 At. % are attributed to Co^{2+} (BEs= 788.35 and 801.86 eV) [46]. Whereas, the Ni 2p spectrum as clarified in **Figure 2(b')** exhibited four obvious main peaks at 856.27, 860.76,868.25, and 873.75 eV, which are ascribed to the Ni $2p_{3/2}$ and Ni $2p_{1/2}$ with one shake-up satellite peak at 864.31 and eV that was assigned to Ni^{2+}[47, 48].

The Mn 2p spectrum as illustrated in **Figure 2(c')** showed the existence of BEs at 637.2 and 647.6 eV that related to Mn $2p_{3/2}$ and Mn $2p_{1/2}$, respectively [49]. Moreover, the spin-orbitals could be deconvoluted into four peaks, two of which are related to Mn^{2+} (BEs= 641.24 and 650 eV) with an intensity of about 63.56 At. %. Additional peaks at BEs of 645.68 and 653.5eV corresponding to Mn^{4+} (36.44 At. %).Hence, the physical mixture oxides are composed of a triple oxide of Mn^{2+}, $Mn^{4+,}$ and W^{6+}. Furthermore, as revealed in **Figure 2(d')**, the Zn 2p spectrum is separated into Zn $2p_{3/2}$ and Zn $2p_{1/2}$, which are located at BEs of 1022.18 and 1045.06 eV, respectively. Their spin-orbit separation is approximately 22.88 eV between them, which corresponds to the Zn^{2+} [50–52]. These results coincided with the findings for pure ZnO and are in line with Bigiani Lorenzo et al. [53]. The Fe2p (**Figure 2(e'))** revealed two spin-orbit doublets for Fe $2p_{3/2}$ and Fe $2p_{1/2}$ at 709.1 and 722.5 eV, respectively. The located BEs at 710.91, 713.8, 717.41, 720.92, and 728.67 eV evidenced the presence of Fe^{3+}[54]. Moreover, the presence of broad satellite peaks at 724.85 and 733.48 eV, matches the Fe $^{3+}$ oxidation state. Moreover, the presence of broad satellite peaks at 717.41, 720.92, and 733.48 eV, matches the Fe $^{3+}$ oxidation state. It could be confirmed the successful double oxide preparation of Co ($^{2+}$ and $^{3+}$), Ni^{2+},Mn($^{2+}$ and $^{4+}$), Zn^{2+}, or Fe^{3+} with $W^{6+}$by a one-step hydrothermal method that is consistent with the XRD results. Furthermore, the electronic interaction between double oxides is significantly effective in enhancing the oxygen evolution efficiency, in addition to the increase in the effective surface area of the prepared electrode [55].

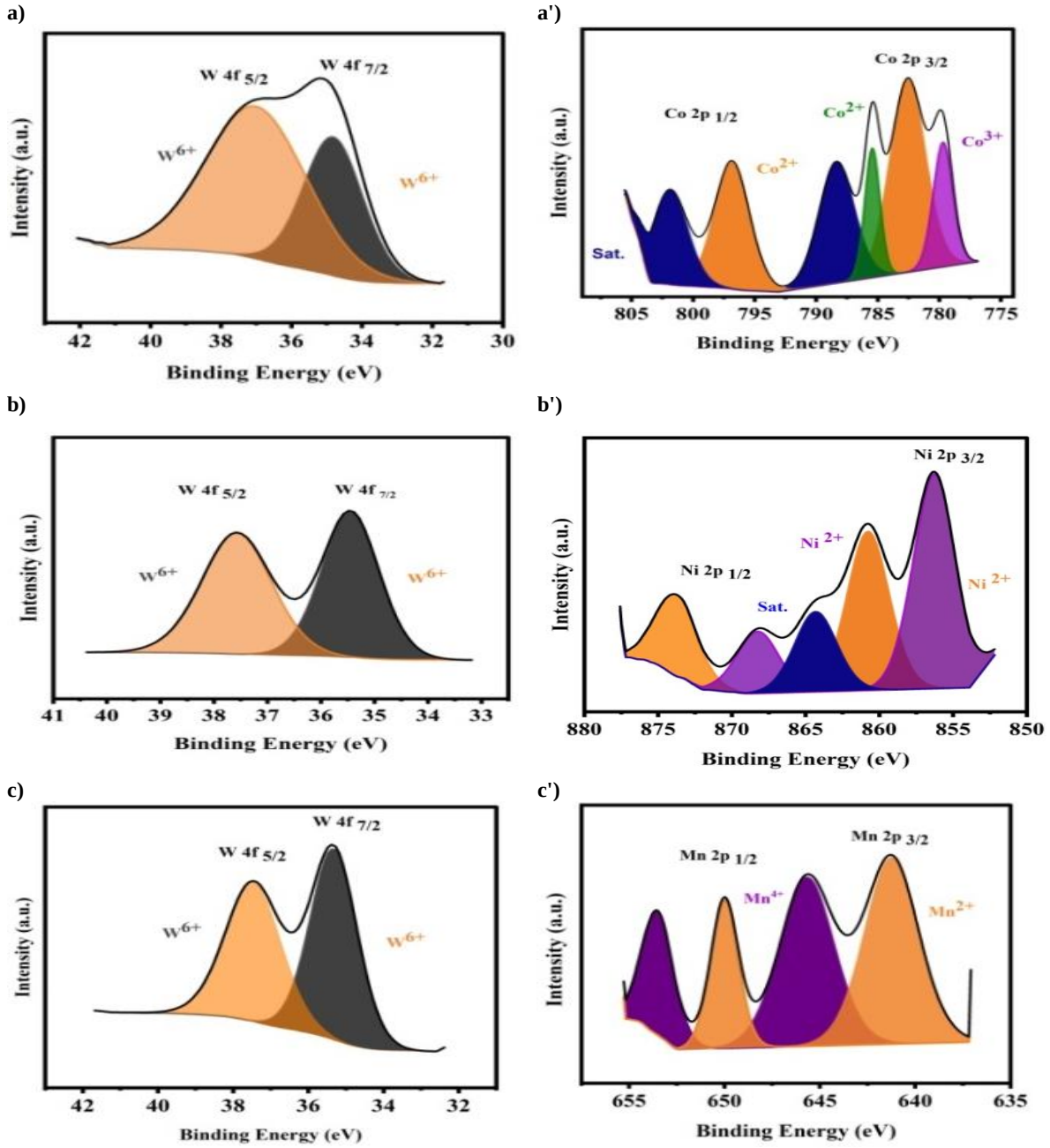

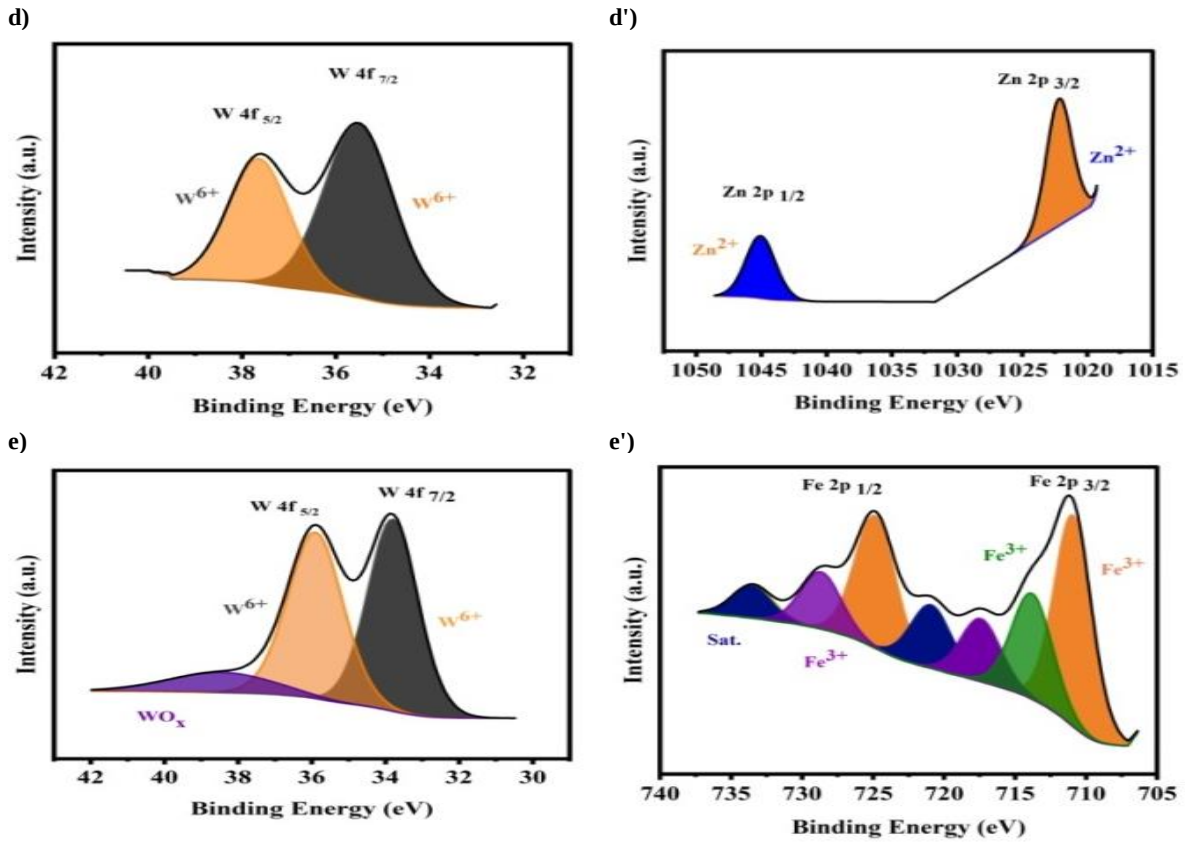

Figure 2: XPS spectra of (a-e) W 4f, a') Co2p, b') Ni 2p, c') Mn 2p, d') Zn 2p and e') Fe2p for $CoWO_4$/rGO-ST, $NiWO_4$/rGO-ST, $MnWO_4$/rGO-ST, $ZnWO_4$/rGO-ST and $Fe_2(WO_4)_3$/rGO-ST electrocatalysts, respectively.

The morphology and microstructure of the $CoWO_4$/rGO-ST, $NiWO_4$/rGO-ST, $MnWO_4$/rGO-ST, $ZnWO_4$/rGO-ST, and $Fe_2(WO_4)_3$/rGO-ST electrocatalysts are investigated by scanning electron microscopy (SEM). Two different magnifications for each electrocatalyst are represented in **Figure 3**. It could be observed that the presence of different transition metals combined with tungsten leads to different morphologies. Generally, the white particles are related to the silica template. Furthermore, $Fe_2(WO_4)_3$/rGO-ST exhibits a dense distribution of these particles.

A homogenous distribution of particles over the substrate (rGO + ST) is observed for the electrocatalysts. EDAX spectra and elemental composition of metal tungstate's electrocatalysts are represented in **Figure 3 (f-j)**.All spectra exhibited peaks for tungsten (W), carbon (C), oxygen (O), and silicon (Si). Moreover, peaks for Co, Ni, Mn, Zn, and Fe are also represented in **Figure 3 (f-j)** respectively. This confirms the presence of nominal metals, as well as the lack of other impurities.The weight and atomic percentages of different elements in the prepared electrocatalysts are illustrated in Table S1(a-e), the results revealed that the presence of mixed support (rGO+ST) reached almost 70% in all electrocatalysts (as the nominal percentage), in a general point of view, an exact stoichiometry of the tungstate's cannot be extracted from the EDAX due to the presence of oxygen also in of mixed support (rGO+ST) and the qualitative nature of EDAX [56].

Transmission electron microscope images for the metal tungsten electrocatalysts are shown in **Figure 4** shows two magnifications of $CoWO_4$/rGO-ST, $NiWO_4$/rGO-ST, $MnWO_4$/rGO-ST, $ZnWO_4$/rGO-ST and $Fe_2(WO_4)_3$/rGO-ST. It could be noticed that the presence of round particles, which could be related to the silica template, and much smaller particles that are related to the nanoparticles of the electrocatalysts are observed with a homogenous distribution over the matrix. It observed the existence of small nanoparticles on the silica particles, especially in $CoWO_4$/rGO-ST and $NiWO_4$/rGO-ST images. A very good distribution of small nanoparticles over the support materials is observed for $MnWO_4$/rGO-ST(2-10 nm). Some agglomeration is also observed as in the cases of $ZnWO_4$/rGO-ST and $Fe_2(WO_4)_3$/rGO-ST. The particle size range of different electrocatalysts are for $CoWO_4$/rGO-ST (11-20 nm), $NiWO_4$/rGO-ST (8-17 nm), $MnWO_4$/rGO-ST (2-10 nm), $ZnWO_4$/rGO-ST (10-25 nm) and $Fe_2(WO_4)_3$/rGO-ST (6-10 nm).

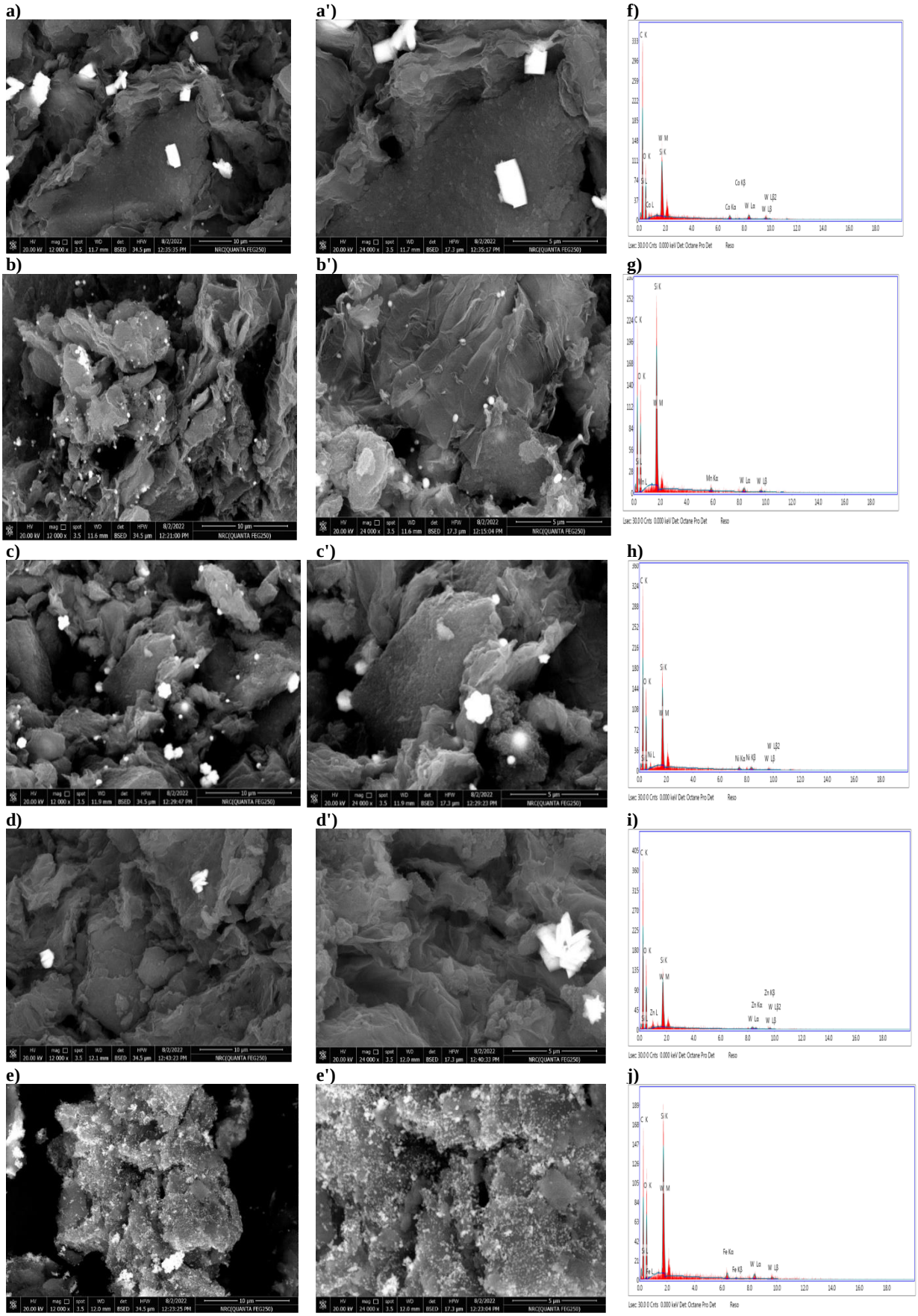

Figure 3: SEM and EDAX analysis of $CoWO_4$/rGO-ST (a, a', f), $NiWO_4$/rGO-ST (b, b',g), $MnWO_4$/rGO-ST (c,c',h), $ZnWO_4$/rGO-ST (d,d',i), $Fe_2(WO_4)_3$/rGO-ST (e, e',j) electrocatalysts.

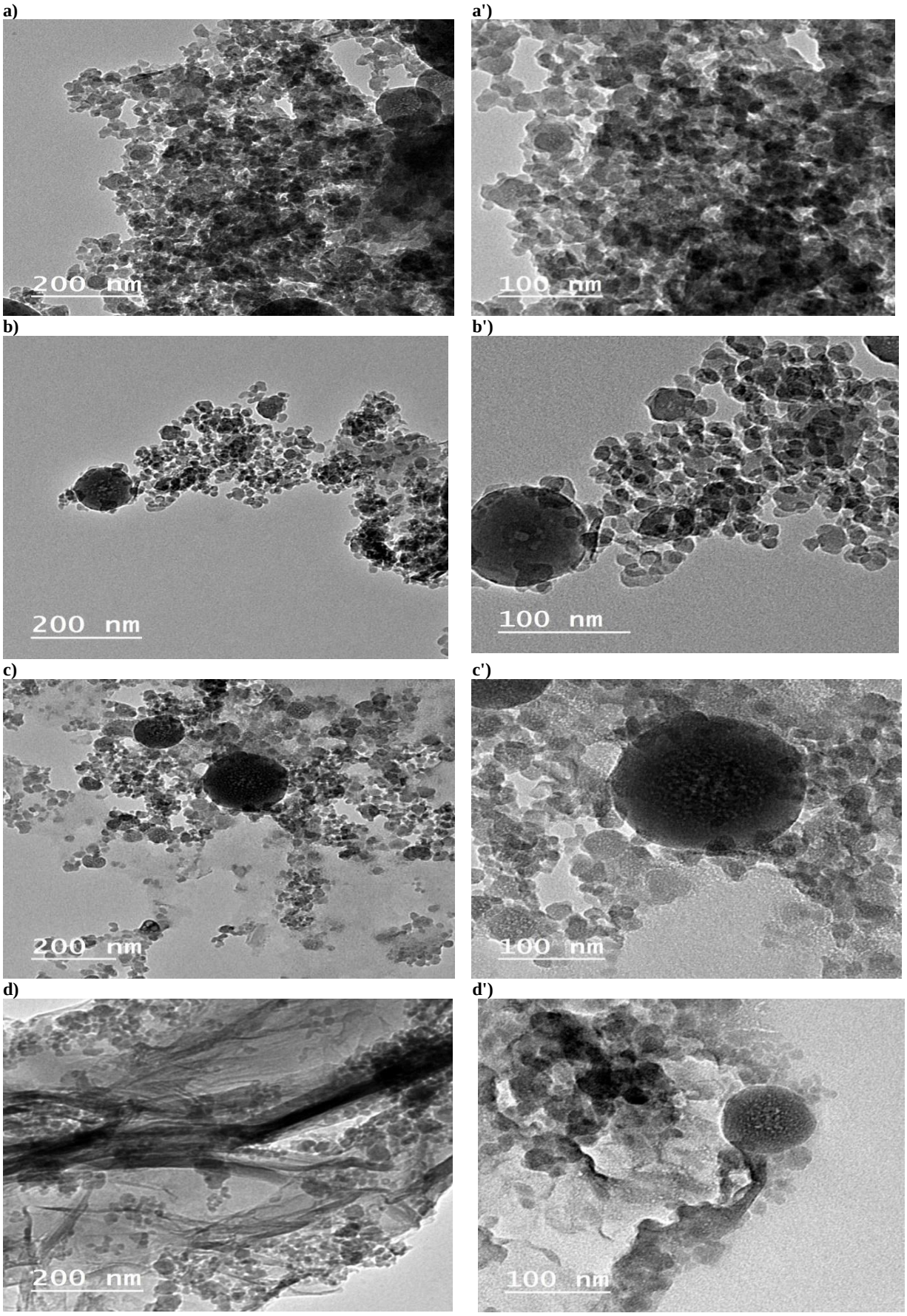
a)
a')
200 nm
100 nm
b)
b')
200 nm
100 nm
c)
c')
200 nm
100 nm
d)
d')
200 nm
100 nm

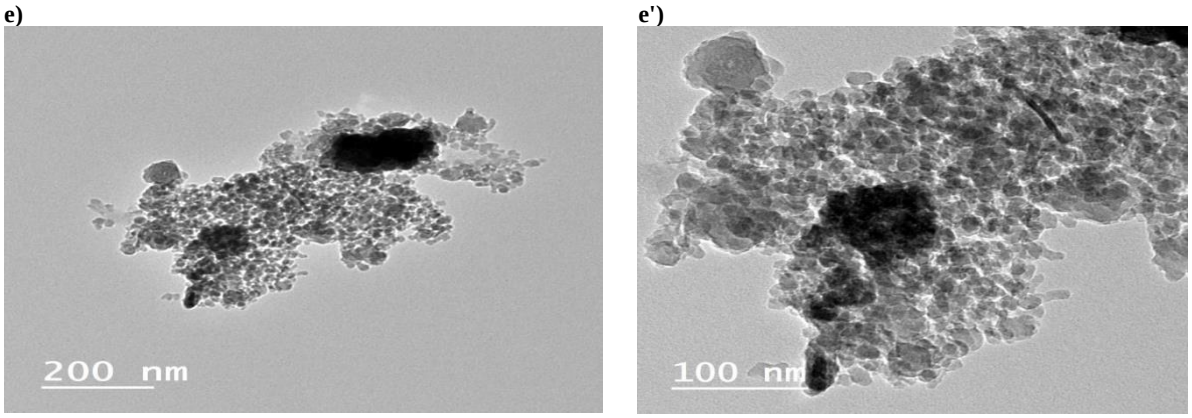

Figure 4: HT-TEM of $CoWO_4$/rGO-ST (a, a'), $NiWO_4$/rGO-ST (b, b'), $MnWO_4$/rGO-ST (c,c'), $ZnWO_4$/rGO-ST (d,d'), $Fe_2(WO_4)_3$/rGO-ST (e, e',) electrocatalysts.

Electrochemical characterization

HER performance

The HER performance of the transition metal tungstate's electrocatalysts is investigated. Linear sweep voltammetry (LSV) is used to measure polarization curves for HER at a scan rate of 5 mV s^{-1} in 1.0 M KOH. The results are corrected using the iR correction. Nickel foam (NF) is used as a carrier for the prepared electrocatalysts due to its high porosity which enables the electrolyte contact in a better way [15]. Figure 5(a) illustrates the linear scanning voltammetry (LSV) of $CoWO_4$/rGO-ST/NF, $NiWO_4$/rGO-ST/NF, $MnWO_4$/rGO-ST/NF, $ZnWO_4$/rGO-ST/NF and $Fe_2(WO_4)_3$/rGO-ST/NF. At a current density of 10 and 50 mA cm^{-2}, $MnWO_4$-rGO-ST/NF has the lowest overpotential values of 150 and 232 mV respectively among the other tested electrocatalysts. Figure 5 (b) shows the histogram of overpotential values of different transition metal tungstate's at current densities of 10 and 50 mA cm^{-2}. It could be observed that the overpotential values at 10 mA cm^{-2}increase in the order of$MnWO_4$/rGO-ST/NF (150 mV) < $NiWO_4$/rGO-ST/NF (174 mV) < $Fe_2(WO_4)_3$/rGO-ST/NF (259 mV) <$CoWO_4$/rGO-ST/NF (280 mV) < $ZnWO_4$/rGO-ST/NF (308 mV)< Ni Foam bare (223 mV). While the overpotential values of the electrocatalysts at 50 mA cm^{-2} follow the order, $MnWO_4$/rGO-ST/NF (232 mV) < $NiWO_4$/rGO-ST/NF (251mV) <$Fe_2(WO_4)_3$/rGO-ST/NF (373 mV)< $ZnWO_4$/rGO-ST/NF (395 mV)< $CoWO_4$/rGO-ST/NF (439 mV), respectively. We can see from Figure 5 (a&b) that the presence of Manganese leads to a significant improvement in the HER activity of other non-precious metal electrocatalysts.

Another method for assessing an electrocatalyst's activity in HER is the Tafel plot, which quantifies the potential needed to drive a decade of reactions. Generally, the lower the Tafel slope, the faster the reaction kinetics. The values of the Tafel slopes used to determine the kinetics and the proposed mechanism of the reaction, including the rate determination step [57]. Additionally, the charge transfer coefficient and the Tafel slope are proportionate, so if a given electrocatalyst has a small value of the Tafel slope, this means that the charge mobility is high. Tafel slopes of the tested electrocatalysts is shown in Figure 5(c), $MnWO_4$/rGO-ST/NF has a Tafel slope of 108 mV dec^{-1}, which is significantly lower than the Tafel slopes of the other electrocatalysts, which are 124, 114, 135, 161, and 229 mV dec^{-1} for Ni Foam are, $NiWO_4$/rGO-ST/NF, $Fe_2(WO_4)_3$-rGO-ST/NF, $ZnWO_4$/rGO-ST/NF, and $CoWO_4$/rGO-ST/NF, respectively. It indicates that $MnWO_4$-rGO-ST/NF has favourable electron transfer kinetics.

From a general point of view, the hydrogen evolution reaction in an alkaline medium involves the following steps: firstly, reduction of H_2O into H* atoms and OH^- ions and this step called the Volmer step and are represented in the following equations [58]:

$$H_2O + e^- \rightarrow H^* + OH^- \quad (1)$$

The second step is the processes of hydrogen desorption to form H_2, this step could be performed through electrochemical desorption which is called the Heyrovsky step:

$$H^* + H_2O + e^- \rightarrow H_2 + OH^- \quad (2)$$

or Tafel reaction which is the chemical desorption step: $2H^* \rightarrow H_2$ (3)

Tafel slopes around 120 mV dec^{-1} suggest a Volmer-Hyrovsky pathway [59].Moreover, this indicates that the Volmer reaction is the rate-determining step. This situation is correct for $MnWO_4$/rGO-ST/NF and $NiWO_4$/rGO-ST/NF. Furthermore, as indicated in Figure 5(d) and Table 1, an EIS analysis is carried out to look into the electron-transfer kinetics for the HER of each sample.The charge transfers resistance (R_{ct}) of $MnWO_4$-rGO-ST/NF is 7.8 Ω which is the lowest value compared to other electrocatalyst, e.g. $CoWO_4$-rGO-ST/NF (46.3 Ω), $NiWO_4$-rGO-ST/NF (8.31 Ω), $ZnWO_4$-rGO-ST/NF (42.15 Ω) and$Fe_2(WO_4)_3$-rGO-ST/NF (31.4 Ω). $MnWO_4$-rGO-ST/NF has faster charge transfer and better electron conductivity, as indicated by the lower Rct value. As a result, during the HER process, electrons can move between the

electrocatalyst and the electrolyte directly and effectively, increasing HER activity. The formation of a heterostructure by $MnWO_4$-rGO-ST/NF can be used to explain this phenomenon, as it leads to lower charge transfer resistance, lower apparent activation energy, and improved electronic conductivity. A chronopotentiometry test is used at a current density -10 mA $cm^{-2}$to assess the stability of various electrocatalyst samples in order to determine their potential applications. Figure 5(e) shows that following 60 hours of stability testing, there was no discernible decline in the current density, indicating the electrocatalyst's excellent stability during HER. Figure S2 shows the normalized decay potential percent with time, the results revealed that the normalized potential decay/increase after 60 hrs is around 5%.The double-layer capacitance (Cdl) of an electrocatalyst is used to calculate its electrochemical surface area using the following formula: ECSA=Cdl/Cs, Where Cs is the specific capacitance (40 mF cm^{-2}) [60]. Based on CV diagrams at various scanning rates (40-200 mVs^{-1}), the Cdl values are obtained as illustrated in **Figure 5(f)**.$MnWO_4$/rGO-ST/NF had the highest C_{dl}value (2.53 mF cm^{-2}) among the other electrocatalysts where their C_{dl} values are 0.36, 1.42, 0.53, 0.53 mF $cm^{-2}$for $CoWO_4$/rGO-ST/NF, $NiWO_4$/rGO-ST/NF, $ZnWO_4$/rGO-ST/NF and $Fe_2(WO_4)_3$/rGO-ST/NF respectively. Larger C_{dl} values mean larger ECSA and exposure to more active sites that lead to higher activity towards HER.

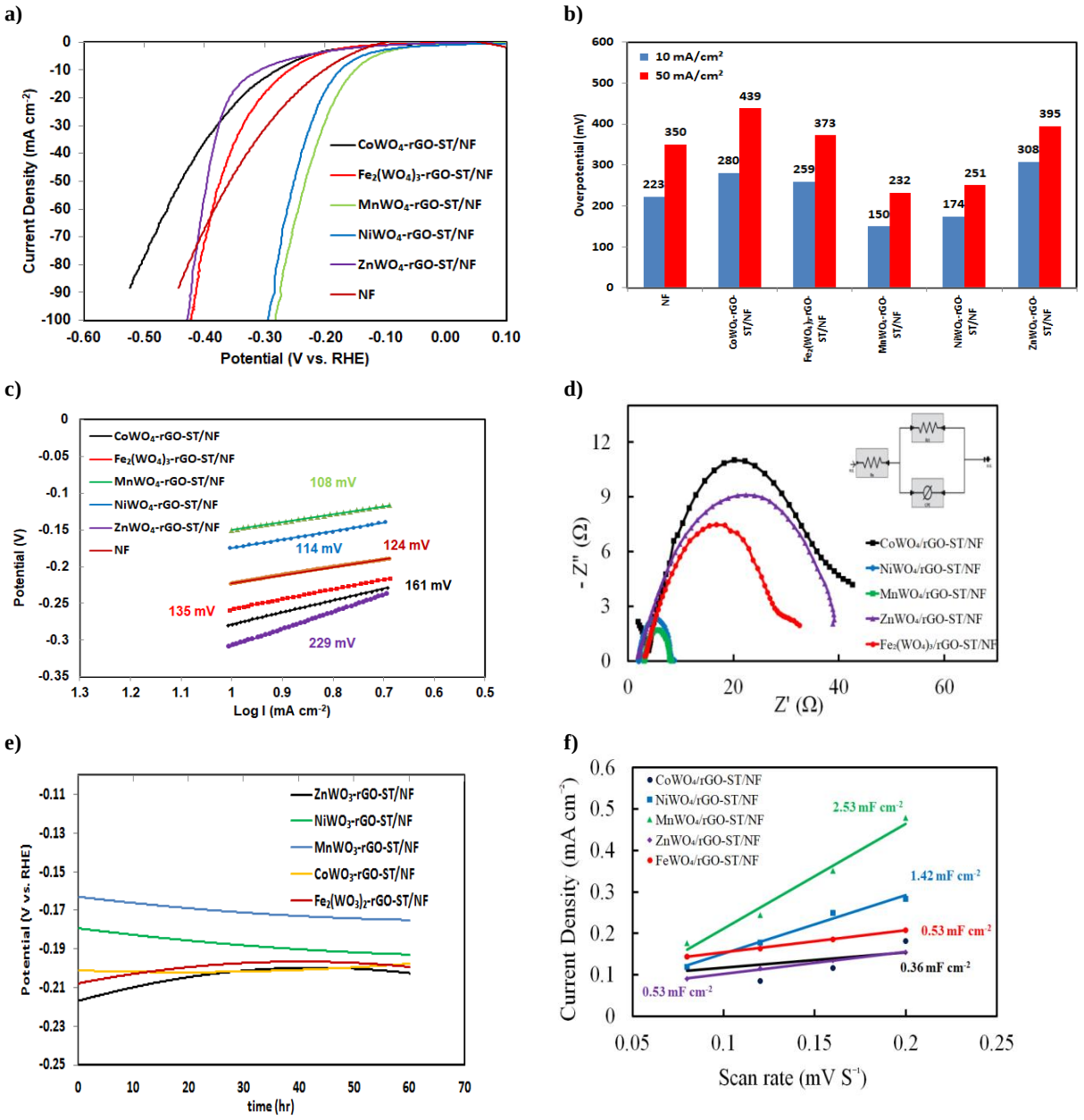

Figure 5:HER performance of the $CoWO_4$/rGO-ST, $NiWO_4$/rGO-ST, $MnWO_4$/rGO-ST, $ZnWO_4$/rGO-ST, $Fe_2(WO_4)_3$/rGO-ST electrocatalysts. (a) LSV curves, (b) Comparison of the overpotential at 10 and 50 mA cm^{-2}, (c) Tafel plots derived from LSV curves, (d)Nyquist plots, (e)chronopotentiometry at -10 mA cm^{-2} (CP) curve, and (f) the double-layer capacitance (Cdl) plots.

From the former results, we could conclude that the presence of Mn and W together in $MnWO_4$/rGO-ST/NF enhances the performance of the electrocatalyst towards HER in the alkaline medium as it has the lowest values of overpotential, Tafel slope, and charge transfer resistance, moreover, it has excellent stability. It is well known that manganese-based electrocatalysts have a lot of active sites; moreover, the presence of another metal such as tungsten could induce a synergistic effect that changes the electronic structure of the electrocatalyst leading to modifications of the binding energy of the intermediates to reach a moderate level and enhance the catalytic activity [61, 62]. Another important factor affecting the performance is presence of the reduced graphene oxide as a supporting material, which can increase the surface area, enhance charge transfer, and improve the corrosion resistance and stability of an electrocatalyst.

Table 1.Rs, Rct and CPE values for $CoWO_4$/rGO-ST/NF, $NiWO_4$/rGO-ST/NF, $MnWO_4$/rGO-ST/NF, $ZnWO_4$/rGO-ST/NF &$Fe_2(WO_4)_3$/rGO-ST/NF for HER.

Electrocatalyst	Rs (Ω)	Rct	CPE	
			Y0	alpha
$CoWO_4$/rGO-ST/NF	2.85	46.3	3.95E-03	0.5599
$NiWO_4$/rGO-ST/NF	2.09	8.31	1.25E-03	0.8147
$MnWO_4$/rGO-ST/NF	3.14	7.8	1.82E-03	0.7721
$ZnWO_4$/rGO-ST/NF	1.70	42.15	2.36E-03	0.5387
$Fe_2(WO_4)_3$/rGO-ST/NF	3.19	31.4	2.06E-03	0.6061

OER Performance

In an O_2-saturated 1.0 M KOH solution, the OER activities of prepared electrocatalysts are assessed using a standard three-electrode setup. Applying linear sweep voltammetry (LSV) at 5 mV s^{-1} sweep rate. All potential values of OER are referenced to the reversible hydrogen electrode moreover;polarization curves for OER are corrected with iR compensation.As shown in **Figure 6 (a)**, the linear voltammetry (LSV) curves of electrocatalysts show that the overpotential of $Fe_2(WO_4)_3$/rGO-ST/NF is 322 mV at a current density of 10 mA cm^{-2}, while other electrocatalyst $MnWO_4$/rGO-ST/NF, $ZnWO_4$/rGO-ST/NF,$CoWO_4$/rGO-ST/NF and $NiWO_4$/rGO-ST/NF, Ni Foam barerequire the overpotential of 325, 348, 358, 390 mV&422 mV, respectively at the current density of 10 mA cm^{-2}, suggesting that $Fe_2(WO_4)_3$/rGO-ST/NF is a highly active electrocatalyst for OER. It is worth noting that the overpotential of $Fe_2(WO_4)_3$/rGO-ST/NFisonly 339 and 351 mV at current densities of 30 and 50 mA cm^{-2}, respectively, which are also much less than that of other electrocatalysts **(Figure 6 (b))**. The OER mechanism includes the transfer of four electrons through four steps as follows: firstly,the dissociation of water molecules on the active sites of the electrocatalyst to form two protons one giving OH* and the other proton forming O* [63]. Secondly, another form HOO* through a nucleophilic attack on O*, and this step is followed by the formation of oxygen gas.

$$M_{ad} + OH^- \rightarrow M_{ad}OH \quad (4)$$

$$M_{ad}OH + OH^- \rightarrow M_{ad}O + H_2O \quad (5)$$

$$M_{ad}O + OH^- \rightarrow M_{ad}OOH + e^- \quad (6)$$

$$M_{ad}OOH + OH^- \rightarrow M_{ad} + O_2 + H_2O \quad (7)$$

Where M is the surface adsorption active sites

Generally, the activity of metal tungstate towards the alkaline OER could be attributed to the presence of tungsten which is considered a high valence transition metal (W^{+6}) that could rearrange the electronic structure of the second transition metals (i.e. Co, Ni, Mn, Zn and Fe), leading to improve the adsorption energy of some intermediates such as OH*, O* and HOO*and the metal ions.Chizhong Wang et al. [64]prepared FeW mixed oxides prepared by a hydrothermal method and tested them for OER in an alkaline medium. They stated that, regarding the presence of Fe with W in metal tungstate, the theoretical calculation has proved that this facilitates the transformation of *OH to *O intermediates, enhancing the OER activity of the electrocatalysts in an alkaline medium.

In order to comprehend the catalytic kinetics, Figure 6(c) displays the Tafel plots. $Fe_2(WO_4)_3$-rGO-ST/NF displays a Tafel slope of 44 mV dec^{-1}, significantly less than that of $CoWO_4$-rGO-ST/NF (130 mV dec^{-1}). The catalytic kinetics of $Fe_2(WO_4)_3$-rGO-ST/NF are more favourable than those of $MnWO_4$-rGO-ST/NF (135 mV dec^{-1}), $NiWO_4$-rGO-ST/NF (144 mV dec^{-1}), $ZnWO_4$-rGO-ST/NF (85 mV dec^{-1}),and Ni Foam (200 mV dec^{-1}) Under OER conditions, electrochemical impedance spectroscopy (EIS) is used to examine the electrocatalytic charge transfer resistances (Rct) at the interface of the electrolyte and catalysts (Figure 6(d)) and Table 2. When compared to $CoWO_4$-rGO-ST/NF (6.93 Ω), $NiWO_4$-rGO-ST/NF (27.83 Ω), $MnWO_4$-rGO-ST/NF (8.1 Ω), and $ZnWO_4$-rGO-ST/NF (14.64 Ω), it is evident that $Fe_2(WO_4)_3$-rGO-ST/NF has the smallest charge-transfer resistance (Rct) value (4.48 Ω). This indicates the exceptional charge transfer efficiency during electrocatalysis. The reason might be that $Fe_2(WO_4)_3$/rGO-ST/NF's structure can reveal a lot of active sites and encourage electrocatalysts to come into contact with electrolyte ions. Excellent stability is also noticed for $Fe_2(WO_4)_3$/rGO-ST/NF in **Figure 6(e)** where there is no decay of potential with time during the entire test period; moreover, it had the best electrochemical surface area (10.71 mF cm^{-2}) among the other electrocatalysts as shown in **Figure 6(f).**Figure S3 shows the normalized decay potential percent with time, the results revealed that the normalized potential decay/increase after 60 hrs around 3%.

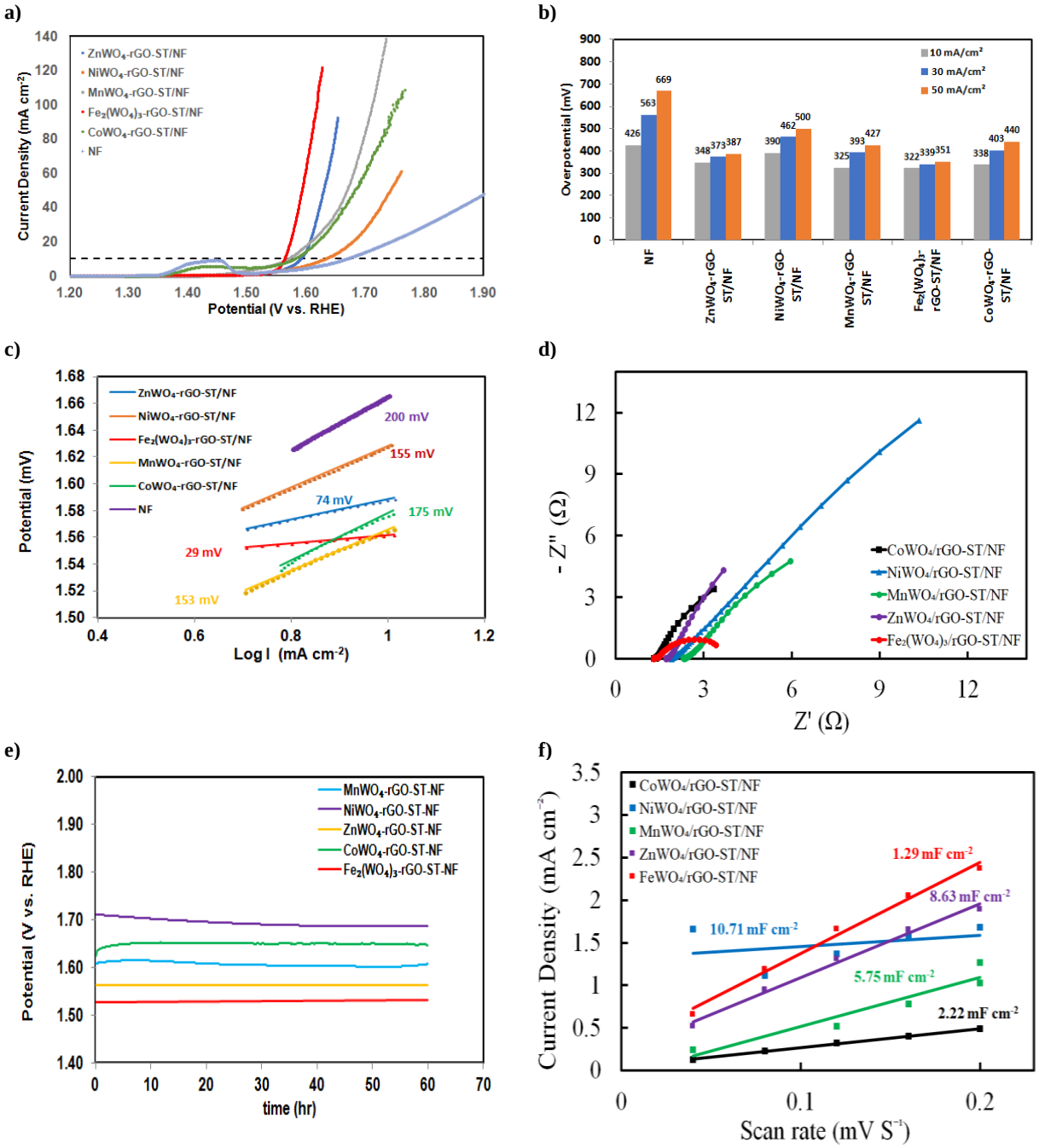

Figure 6: OER performance of the $CoWO_4$/rGO-ST, $NiWO_4$/rGO-ST, $MnWO_4$/rGO-ST, $ZnWO_4$/rGO-ST, $Fe_2(WO_4)_3$/rGO-ST electrocatalysts. (a) LSV curves, (b) Comparison of the overpotential at 10, 30, and 50 mA cm^{-2}, (c) Tafel plots derived from LSV curves, (d) Nyquist plots, (e) chronopotentiometry at 10 mA cm^{-2}(CP) curve, and (f) the double-layer capacitance (Cdl) plots.

Table 2: Rs, Rct and CPE values for $CoWO_4$/rGO-ST/NF, $NiWO_4$/rGO-ST/NF, $MnWO_4$/rGO-ST/NF, $ZnWO_4$/rGO-ST/NFand$Fe_2(WO_4)_3$-rGO-ST/NF for OER.

Electrocatalyst	Rs (Ω)	Rct	W	CPE	
				Y0	alpha
$CoWO_4$/rGO-ST/NF	1.33	6.93	0.953	0.5365	1.0
$NiWO_4$/rGO-ST/NF	1.90	27.83	0.169	0.016	0.874
$MnWO_4$/rGO-ST/NF	2.36	8.10	0.376	0.536	1.0
$ZnWO_4$/rGO-ST/NF	1.73	14.64	0.782	0.466	1.0
$Fe_2(WO_4)_3$/rGO-ST/NF	1.35	4.48	-	0.263	0.675

To the best of our knowledge, the prepared electrocatalysts with these novel designs (MWO_4/rGO-ST) have not been tested in the literature for water splitting in an alkaline medium, however, there are a few related electrocatalysts in the literature listed in **Table 3** to compare with.

Table (3) represents a performance comparison with recently published non-noble metal-based for HER & OER electrocatalysts,for example,Xiaoqiang Du et al [23] prepared $NiCo_2O_4$@$NiWO_4$ core-shell nanorods arrays on nickel foam, they found that the electrocatalyst has an overpotential of only 310 mV at 10 mA cm^{-2} , this performance is related to the presence of nickel foam during catalyst growth which considered as three-dimensional porous conductive substrates, that leads to increase the surface area and improve the rate of diffusion of gases. Moreover, there is a synergetic effect between $NiCo_2O_4$ and $NiWO_4$. Fang Luoa et al. [65] stated that $CoWO_4$-x@C electrocatalysts have good OER activity because of the presence of oxygen vacancies formed by H_2 annealing at different temperatures, oxygen vacancies facilitated the adsorption of OH^-species. Moreover, SangeethaKumaravelet al. [66] prepared cobalt tungsten oxide hydroxide hydrate (CTOHH) on a deoxyribonucleic acid (DNA) scaffold by microwave heating method. In OER, at a current density of 10 mA cm^{-2}, CTOHH-DNA required an overpotential of 355 mV which is a higher value than our $CoWO_4$/rGO-ST/NF(338 mV) as stated in Table (3), whereas CTOHH, $CoWO_4$ on DNA scaffold, and$CoWO_4$have higher overpotential of 372, 443, and480 mV, respectively, The authors stated that lower activities of the other electrocatalysts is related to their high charge transfer resistance.

Other electrocatalysts for OER that combined W, Co, and Mn were prepared by GuruprakashKarkeraet al. [67], the authors revealed that in $Co_{0.5}Mn_{0.5}WO_4$, Co, and Mn 3d orbitals in the conduction and valance band stay near to the Fermi level, that account for high electrochemical activity. However, as shown in table (3) our prepared electrocatalysts have lower overpotential values at 10 mA cm^{-2}. As examples of HER electrocatalysts, SO-strontium tungstate has an overpotential of 660 mV at 10 mA cm^{-2} [68] when this result is compared to the performance of all prepared electrocatalysts, they have better performance towards HER in an alkaline medium, however, the authors stated that for $SrWO_4$, each of the W-ions is present within tetrahedral cages and isolated together, while the octahedral unit of Sr-ions is surrounded by eight oxygen ions and this situation can leads to a structural disorder such as the formation of oxygen vacancies. Furthermore, KaruppaiahSelvakumar [71] developed tungsten/cobalt oxide supported on the TiO_2-rGO catalyst (TPWCoR),the good performance of the electrocatalyst is related to its higher number of active sites, where at 10 mA cm^{-2}, and it has overpotential of 144 mV for HER and 366 mV for OER in alkaline medium. Our electrocatalyst $MnWO_4$/rGO-ST/NF displayed a comparable overpotential to TPWCoR (150@10 mA cm^{-2}) in the case of HER and at the same time, it has a better performance for OER (325@10 mA cm^{-2}).

Water splitting

Based on the HER and OER performance of the tested electrocatalyst, the best electrocatalyst performance for HER and OER is selected for the water-splitting system evaluation. Using $MnWO_4$/rGO-ST/NF as the anode and $Fe_2(WO_4)_3$/rGO-ST/NF as the cathode, the water electrolysis cell is assembled, and the overall water splitting performance is further examined in 1M KOH. The $MnWO_4$/rGO-ST/NF||$Fe_2(WO_4)_3$/rGO-ST/NF device, as assembled, exhibits a good overall water splitting performance with cell voltages of approximately 1.81 V at a current density of 10 mA cm^{-2} for a 12-hour period, as illustrated in Figure 7.

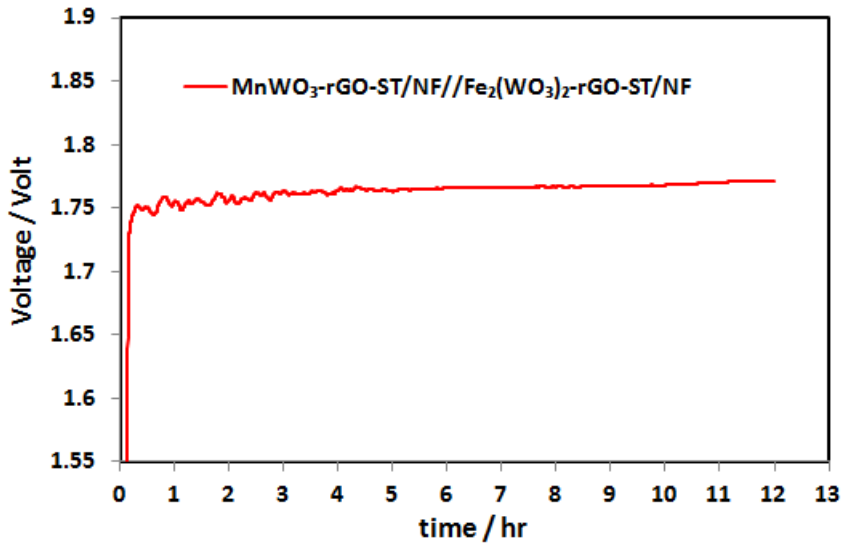

Figure 7: Chronopotentiometry(CP) stability test for $MnWO_4$-rGO-ST/NF||$Fe_2(WO_4)_3$-rGO-ST/NF water splitting system.

Table 3. Performance comparison with recently published non-noble metal-based for HER & OER electrocatalysts.

Electrocatalyst	HER		OER		Ref
	Over potential Ƞ (mV)	Tafel slopes mV dec^{-1}	Over potential ƞ(mV)	Tafel slopes mV dec^{-1}	
$CoWO_4$/rGO-ST/NF	280@10 mA cm^{-2} 439@50 mA cm^{-2}	259	338@10 mA cm^{-2} 403@30 mA cm^{-2} 440@50 mA cm^{-2}	130	Current study
$NiWO_4$/rGO-ST/NF	174@10 mA cm^{-2} 251@50 mA cm^{-2}	135	390@10 mA cm^{-2} 462@30 mA cm^{-2} 500@50 mA cm^{-2}	144	Current study
$MnWO_4$/rGO-ST/NF	150@10 mA cm^{-2} 232@50 mA cm^{-2}	130	325@10 mA cm^{-2} 393@30 mA cm^{-2} 427@50 mA cm^{-2}	135	Current study
$ZnWO_4$/rGO-ST/NF	308@10 mA cm^{-2} 395@50 mA cm^{-2}	191	348@10 mA cm^{-2} 373@30 mA cm^{-2} 387@50 mA cm^{-2}	85	Current study
$Fe_2(WO_4)_3$/rGO-ST/NF	259@10 mA cm^{-2} 373@50 mA cm^{-2}	185	322@10 mA cm^{-2} 339@30 mA cm^{-2} 351@50 mA cm^{-2}	44	Current study
$NiCo_2O_4$@$NiWO_4$/NF			310@10 mA cm^{-2}	102.8	[23]
$Fe_{0.95}W_{0.05}$			430 @10 mA cm^{-2}	49.6	[64]
Fe3W1			410@10 mA cm^{-2}	51.7	
Fe1W1			440@10 mA cm^{-2}	53.4	
Fe1W3			440@10 mA cm^{-2}	55.5	
$CoWO_{4-x}$@C-0			374@10 mA cm^{-2}		[65]
$CoWO_{4-x}$@C-2			354@10 mA cm^{-2}		
$CoWO_{4-x}$@C-4			295@10 mA cm^{-2}		
$CoWO_{4-x}$@C-6			304@10 mA cm^{-2}		
Cobalt Tungsten Oxide Hydroxide hydrate) CTOHH-DNA CTOHH $CoWO_4$ on DNA scaffold $CoWO_4$	-	-	355 @10 mA cm^{-2} 372@10 mA cm^{-2} 443@10 mA cm^{-2} 480@10 mA cm^{-2}	48 47.5 84 90	[66]
$Co_{0.5}Mn_{0.5}WO_4$			400 @10 mA cm^{-2}	80	[67]
$Co_{0.75}Mn_{0.25}WO_4$			500@10 mA cm^{-2}	100	
$CoWO_4$			590@10 mA cm^{-2}	104	
$Co_{0.25}Mn_{0.75}WO_4$			730@10 mA cm^{-2}	142	
SO-$SrWO_4$	660@10 mA cm^{-2}	138	500@10 mA cm^{-2}	218	[68]

$Co_{0.708}Fe_{0.292}WO_4$			327 @10 mA cm^{-2}	53	[69]
$CoWO_4$			421@10 mA cm^{-2}	58	
$FeWO_4$			403@10 mA cm^{-2}	60	
$CoWO_4$ (polyol)			383@10 mA cm^{-2}	51	[70]
$FeWO_4$(polyol)			459@10 mA cm^{-2}	48.8	
$Co_{0.5}Fe_{0.5}WO_4$(polyol)			331 @10 mA cm^{-2}	36.8	
$Co_{0.5}Fe_{0.5}WO_4$(hydrothermal)			360@10 mA cm^{-2}	36.3	
Tungsten/cobalt TiO_2-rGO (TPWCoR**)**	144@10 mA cm^{-2}	114.2	366@10 mA cm^{-2}	62.6	[71]

Conclusion

This paper reports a novel design of low-cost and stable bifunctional electrocatalysts for HER and OER in an alkaline medium. Five different electrocatalysts based on metaltungstate's MWO_4 (M = Co, Ni, Mn, Zn, and Fe) are deposited on a surface composed of reduced graphene oxide and silica template (rGO-ST) via a simple hydrothermal method. XRD and XPS analyses proved the formation of the nominal construction of the electrocatalysts, while TEM and SEM analyses showed the good morphology and distribution of the nanoparticles over the matrix. Furthermore, EDAX has proved the presence of the starting elements. The prepared electrocatalyst exhibits good bifunctional catalytic activity and stability towards HER and OER in an alkaline medium. The most efficient electrocatalyst for HER is $MnWO_4$/rGO-ST/NF, at current densities of 10 and 50 mA cm^{-2}, it requires only overpotential values of 150 and 232 mV respectively (Tafel slope: 130 mV dec^{-1}). In the case of OER, $Fe_2(WO_4)_3$/rGO-ST/NF has the best performance with overpotential values of 322, 339, and 352 mV at 10, 30, and 50 mA cm^{-2} respectively (Tafel slope: 44 mV dec^{-1}). The electrode pair of MnWO/rGO-ST/NF and Fe(WO)/rGO-ST/NF exhibits a cell voltage of 1.81 V, demonstrating superior durability over a 12-hour period for overall water splitting. The good performance may be related to the synergetic effect between tungsten and the transition metals and the presence of support that increases the active surface area.

Fund
The work was financially supported by the Science and Technology Development Fund of Egypt (STDF) (Project No. 43149).

Acknowledgments
The work was financially supported by the Science and Technology Development Fund of Egypt (STDF) (Project No. 43149).

References

[1] A.H. Al-Naggar, N.M.Shinde, J.-S. Kim, R.S.Mane, Water splitting performance of metal and non-metal-doped transition metal oxide electrocatalysts, Coord.Chem. Rev. 474 (2023) 214864.

[2] H. Jin, X. Wang, C. Tang, A. Vasileff, A.S. L. Li, S.Z. Qiao, Stable and highly efficient hydrogen evolution from seawater enabled by an unsaturated nickel surface nitride, Adv. Mater. 33 (2021) 2007508.

[3] L. Yu, Q. Zhu, S. Song, B. McElhenny, D. Wang, C. Wu, Z. Qin, J. Bao, Y. Yu, S. Chen, Non-noble metal-nitride based electrocatalysts for high-performance alkaline seawater electrolysis, Nat. Commun. 10 (2019) 5106.

[4] X. Luo, P. Ji, P. Wang, R. Cheng, D. Chen, C. Lin, J. Zhang, J. He, Z. Shi, N. Li, Interface engineering of hierarchical branched Mo-doped Ni3S2/NixPy hollow heterostructure nanorods for efficient overall water splitting, Adv. Energy Mater. 10 (2020) 1903891.

[5] S. Navalon, A. Dhakshinamoorthy, M. Alvaro, M. Antonietti, H. García, Active sites on graphene-based materials as metal-free catalysts, Chem. Soc. Rev. 46 (2017) 4501–4529.

[6] R. Paul, R. Paul, L. Zhu, H. Chen, J. Qu, L. Dai, Recent advances in carbon-based metal-free electrocatalysts, Adv. Mater. 31 (2019) 1806403.

[7] G.M. Kumar, P. Ilanchezhiyan, C. Siva, A. Madhankumar, T.W. Kang, D.Y. Kim, Electrocatalytic oxygen evolution and photo switching functions of tungsten-titanium binary oxide nanostructures, Appl. Surf. Sci. 496 (2019) 143652. https://doi.org/10.1016/j.apsusc.2019.143652.

[8] D. Li, J. Tu, Y. Lu, B. Zhang, Recent advances in hybrid water electrolysis for energy-saving hydrogen production, Green Chem. Eng. (2022).
[9] T. Zheng, W. Sang, Z. He, Q. Wei, B. Chen, H. Li, C. Cao, R. Huang, X. Yan, B. Pan, Conductive tungsten oxide nanosheets for highly efficient hydrogen evolution, Nano Lett. 17 (2017) 7968–7973.
[10] X. Shang, Y. Rao, S.-S.Lu, B. Dong, L.-M.Zhang, X.-H. Liu, X. Li, Y.-R. Liu, Y.-M.Chai, C.-G.Liu, Novel WS2/WO3 heterostructured nanosheets as efficient electrocatalyst for hydrogen evolution reaction, Mater. Chem. Phys. 197 (2017) 123–128.
[11] Y. Lv, Y. Liu, C. Chen, T. Wang, M. Zhang, Octopus tentacles-like WO3/C@ CoO as high property and long life-time electrocatalyst for hydrogen evolution reaction, Electrochim. Acta. 281 (2018) 1–8.
[12] T.H. Wondimu, G.C. Chen, D.M. Kabtamu, H.Y. Chen, A.W. Bayeh, H.C. Huang, C.H. Wang, Highly efficient and durable phosphine reduced iron-doped tungsten oxide/reduced graphene oxide nanocomposites for the hydrogen evolution reaction, Int. J. Hydrogen Energy. 43 (2018) 6481–6490.
[13] F. Chekin, S. Bagheri, S.B.A. Hamid, Synthesis of tungsten oxide nanorods by the controlling precipitation reaction: application for hydrogen evolution reaction on a WO3 nanorods/carbon nanotubes composite film modified electrode, J. Chinese Chem. Soc. 60 (2013) 447–451.
[14] W. Kong, X. Zhang, S. Liu, Y. Zhou, B. Chang, S. Zhang, H. Fan, B. Yang, N doped carbon dot modified WO3 nanoflakes for efficient photoelectrochemical water oxidation, Adv. Mater. Interfaces.(2019) 1801653.
[15] F. Tang, L. Li, D. Chen, Mesoporous silica nanoparticlessynthesis biocompatibility and drug delivery, Adv. Mater. 24(2012) 1504–1534.
[16] S.H. Wu, C.Y. Mou, H.P. Lin, Synthesis of mesoporous silicananoparticles, Chem. Soc. Rev. 42 (2013) 3862–3875,
[17] X. Fang, Z. Liu, M.F. Hsieh, M. Chen, P. Liu, C. Chen, N. Zheng, ACS Nano 6 (2012)4434-4444.
[18] Y. Zhao, S. Wei, L. Xia, K. Pan, B. Zhang, H. Huang, Z. Dong, H.-H. Wu, J. Lin, H. Pang, Sintered Ni metal as a matrix of robust self-supporting electrode for ultra-stable hydrogen evolution, Chem. Eng. J. 430,133040 (2022).
[19] Niu L, Li Z, Xu Y, Sun J, Hong W, Liu X, Wang J, Yang S. Simple synthesis of amorphous NiWO4 nanostructure and its application as a novel cathode material for asymmetric supercapacitors. ACS Appl Mater Interfaces 2013;5:8044-52.
[20] Lei Y, Li J, Wang Y, Gu L, Chang Y, Yuan H, Xiao D. Rapid microwave-assisted green synthesis of 3D hierarchical flower-shaped NiCo2O4 microsphere for high-performance supercapacitor. ACS Appl Mater Interfaces 2014;6:1773-80.
[21] X. Du, Z. Dai, Y. Wang, X. Han, X. Zhang, Facile synthesis of MWO4 (M= Co, Ni, Zn and Cu) nanoarrays for efficient urea oxidation, Int. J. Hydrogen Energy. 47 (2022) 8875–8882.
[22] X. Yue, Y. Zheng, Y. Chen, S. Huang, Overall water splitting on Ni0. 19WO4 nanowires as highly efficient and durable bifunctional non-precious metal electrocatalysts, Electrochim. Acta.333 (2020) 135554.
[23] X. Du, Q. Shao, X. Zhang, Metal tungstate dominated $NiCo_2O_4$@$NiWO_4$nanorods arrays as an efficient electrocatalyst for water splitting, Int. J. Hydrogen Energy. 44 (2018) 2883–2888.
[24] C. Shu, S. Kang, Y. Jin, X. Yue, P.K. Shen, Bifunctional porous non-precious metal WO2 hexahedral networks as an electrocatalyst for full water splitting, J. Mater. Chem. A. 5 (2017) 9655–9660.
[25] J. Diao, W. Yuan, Y. Qiu, L. Cheng, X. Guo, A hierarchical oxygen vacancy-rich WO3 with “nanowire-array-on-nanosheet-array” structure for highly efficient oxygen evolution reaction, J. Mater. Chem. A. 7 (2019) 6730–6739.
[26] Q. Peng, Q. He, Y. Hu, T.T. Isimjan, R. Hou, X. Yang, Interface engineering of porous Fe2P-WO2. 92 catalyst with oxygen vacancies for highly active and stable large-current oxygen evolution and overall water splitting, J. Energy Chem. 65 (2022) 574–582.
[27] V. Anupama, A.S. Mideen, S. Shibli, Tuning of electrocatalytic activity of WO3–TiO2 nanocomposite electrode for alkaline hydrogen evolution reaction, Int. J. Hydrogen Energy. 46 (2021) 15145–15160.
[28] R.S. Amin, A.E. Fetohi, D.Z. Khater, J. Lin, Y. Wang, C. Wang, K.M. El-Khatib, Selenium-transition metal supported on a mixture of reduced graphene oxide and silica template for water splitting, RSC Adv. 13 (2023) 15856–15871.
[29] M. Samancı, A.B. Yurtcan, Chemically and thermally reduced graphene oxide supported Pt catalysts prepared by supercritical deposition, Int. J. Hydrogen Energy. 47 (2022) 19669–19689.
[30] A. Romero, M. Lavin-Lopez, L. Sanchez-Silva, J. Valverde, A. Paton-Carrero, Comparative study of different scalable routes to synthesize graphene oxide and reduced graphene oxide, Mater. Chem. Phys. 203 (2018) 284–292.
[31] R. Siburian, C. Simanjuntak, M. Supeno, S. Lumbanraja, H. Sihotang, New route to synthesize of graphene nano sheets, (n.d.) 2018.
[32] S. Mgidlana, T. Nyokong, Asymmetrical zinc (II) phthalocyanines cobalt tungstate nanomaterial conjugates for photodegradation of methylene blue, J. Photochem. Photobiol.A Chem. 418 (2021) 113421.

[33] L. Wang, S. Zhu, Y. Wang, Z. Liu, Y. Liu, Q. Wang, M. Gu, K. Li, X. Sun, L. Yang, Amorphous nickel tungstate nanocatalyst boosts urea electrooxidation, Chem. Eng. J. 460 (2023) 141826.

[34] D. Meziani, Y. Roumila, N. Ghoul, D. Benmeriem, K. Abdmeziem, M. Trari, Physicochemical characterizations and semiconducting properties of a manganese tungstate MnWO 4 obtained by hydrothermal route, J. Solid State Electrochem. 25 (2021) 2097–2106.

[35] R.O. Connor, J. Bogan, A. Mccoy, C. Byrne, G. Hughes, R.O. Connor, J. Bogan, A. Mccoy, C. Byrne, G. Hughes, A photoemission study of the effectiveness of nickel, manganese, and cobalt based corrosion barriers for silicon photo-anodes during water oxidation, J. Appl. Phys. 119–195301 (2016) 1–8.

[36] F.Y. Xie, L. Gong, X. Liu, Y.T. Tao, W.H. Zhang, S.H. Chen, H. Meng, J. Chen, XPS studies on surface reduction of tungsten oxide nanowire film by Ar + bombardment, J. Electron Spectros. Relat.Phenomena. 185 (2012) 112–118.

[37] W. Superalloy, A.N. Mansour, K.L. Vasanth, Characterization of W84.9Ni9.5Fe5.6 Super alloy by XPS, Surf. Sci. Spectra. 2 (1993) 76–84.

[38] T.D. Bestwick, G.S. Oehrlein, T.D. Bestwick, S. Gottlieb, Tungsten etching mechanisms in CF4/O2 reactive ion etching plasmas, J. Appl. Phys. 66 (1989) 5034–5038.

[39] P.C. Lemaire, M. King, G.N. Parsons, P.C. Lemaire, M. King, G.N. Parsons, Understanding inherent substrate selectivity during atomic layer deposition: Effect of surface preparation, hydroxyl density , and metal oxide composition on nucleation mechanisms during tungsten ALD, J. Chem. Phys. 146 (2017) 1–9.

[40] D. Barreca, C.I.M.A. Dipartimento, V. Marzolo, G. Carta, C.S. Uniti, A. Gasparotto, V. Loredan, G. Rossetto, C.S. Uniti, E. Tondello, A Study of Nanophase Tungsten Oxides Thin Films by XPS, Surf. Sci. Spectra. 8 (2001) 258–267.

[41] K. Izumiya, E. Akiyama, H. Habazaki, N. Kumagai, A. Kawashima, Anodically deposited manganese oxide and manganese ± tungsten oxide electrodes for oxygen evolution from seawater, Electrochim. Acta.43 (1998) 3303±3312.

[42] D. Schlettwein, M. Becker, Electrochromic switching of tungsten oxide films grown by reactive ion-beam sputter deposition, J Mater Sci. 56 (2021) 615–628.

[43] D.B. Carraro, A. Gasparotto, C. Maccato, D. Barreca, Fe2 O3 -WO3 nanosystems synthesized by a hybrid CVD / sputtering route , and analyzed by X-ray photoelectron spectroscopy, Surf. Sci. Spectra. 23 (2016) 93–101.

[44] H. Wong, J. Zhou, J. Zhang, H. Jin, K. Kakushima, H. Iwai, The interfaces of lanthanum oxide-based subnanometer EOT gate dielectrics, Nanoscale Res. Lett. 9 (2014) 1–5.

[45] Z.C. Sobell, A.S. Cavanagh, S.M. George, Z.C. Sobell, A.S. Cavanagh, S.M. George, Growth of cobalt films at room temperature using sequential exposures of cobalt tricarbonyl nitrosyl and low energy electrons, J. Vac. Sci. Technol. A. 37, 060906 (2019) 1–11.

[46] Z. Zhang, T. Dwyer, S.M. Sirard, J.G. Ekerdt, Z. Zhang, T. Dwyer, S.M. Sirard, J.G. Ekerdt, films Area-selective atomic layer deposition of cobalt oxide to generate patterned cobalt films, J. Vac. Sci. Technol. A. 37, 020905 (2019) 1–9.

[47] D. Guo, J. Lai, F. Cheng, W. Zhao, H. Chen, H. Li, X. Liu, D. Yin, N. Yu, Titanium silicalite-1 supported bimetallic catalysts for selective hydrogenolysis of 5-hydroxymethylfurfural to biofuel 2 , 5-dimethylfuran, Chem. Eng. J. Adv. 5 (2021) 100081.

[48] W. Chen, T. Chang, P. Liu, J. Yeh, C. Tu, J. Lou, C. Yeh, W. Chen, Non-volatile memory characteristics of nickel-silicon-nitride nanocrystal, Appl. Phys. Lett. 91,082103 (2007) 1–3.

[49] Y. Kou, B. Zhang, J. Niu, S. Li, H. Wang, T. Tanaka, S. Yoshida, Amorphous Features of Working Catalysts: XAFS and XPS Characterization of $Mn/Na_2WO_4/SiO_2$ as Used for the Oxidative Coupling of Methane, J. Catal. 408 (1998) 399–408.

[50] F. Qiao, R. Kang, Q. Liang, Y. Cai, J. Bian, X. Hou, Tunability in the Optical and Electronic Properties of ZnSe Microspheres via Ag and Mn Doping, ACS Omega. 4 (2019) 12271–12277.

[51] Y.C. Hong, J.H. Kim, S.C. Cho, H.S. Uhm, Y.C. Hong, J.H. Kim, S.C. Cho, H. Sup, ZnO nanocrystals synthesized by evaporation of Zn in microwave plasma torch in terms of mixture ratio of N2 to O2, Phys. Plasmas. 13, 063506 (2006) 1–6.

[52] A. Ghods, C. Zhou, I.T. Ferguson, XPS characterization of Al2O3/ ZnO ultrathin films grown by atomic layer deposition, Surf. Sci. Spectra. 27, 024012 (2020) 1–8.

[53] L. Bigiani, A. Gasparotto, G. Carraro, C. Maccato, D. Barreca, ZnO-based nanocomposites prepared by a vapor phase route , investigated by XPS, Surf. Sci. Spectra. 25, 024005 (2018) 1–19.

[54] J. Hnát, M. Plevova, R.A. Tufa, J. Zitka, M. Paidar, K. Bouzek, Development and testing of a novel catalyst-coated membrane with platinum-free catalysts for alkaline water electrolysis, Int. J. Hydrogen Energy. 44 (2019) 17493–17504.

[55] A.A. El-Moneim, Mn-Mo-W-oxide anodes for oxygen evolution during seawater electrolysis for hydrogen production : Effect of repeated anodic deposition, Int. J. Hydrogen Energy. 36 (2011) 13398–13406.

[56]D. Valerini, S.Hernández, F.DiBenedetto, N.Russo, G.Saracco, A.Rizzo, SputteredWO3 films forwatersplittingapplications, Materials ScienceinSemiconductorProcessing42(2016)150–154

[57] S. S, S.A. Shanmugapriya S, S. S, K.S. R., Electrospun carbon nanofibers encapsulated with NiCoP: a multifunctional electrode for supercapattery and oxygen reduction, oxygen evolution, and hydrogen evolution reactions, Adv Energy Mater. 8, 1800555 (2018).

[58] S.M. El-Refaei, P.A. Russo, N. Pinna, Recent advances in multimetal and doped transition-metal phosphides for the hydrogen evolution reaction at different pH values, ACS Appl. Mater. 13 (2021) 22077–22097.

[59] W. Jiang, J. Chen, G. Qian, H. He, H. Zhang, X. Zhuo, F. Shen, L. Luo, S. Yin, Interfacial electronic engineering of carbon encapsulated Co 5.47 N-WO2 for boosting overall water splitting, Electrochim. Acta.390, 1388 (2021).

[60] C.C. McCrory, S. Jung, J.C. Peters, T.F. Jaramillo, Benchmarking Heterogeneous Electrocatalysts for the Oxygen Evolution Reaction, J. Am.Chem. Soc. 135 (2013) 16977–16987.

[61] S. Liu, E.H. Zhang, X.D. Wan, R.R. Pan, Y.M. Li, X.M. Zhang, M.Y. Su, J. Liu, J.T. Zhang, Ru-Co-Mntrimetallic alloy nanocatalyst driving bifunctional redox electrocatalysis, Sci. China Math. 65 (2022) 131–138.

[62] K.X. Wang, Y.L. Wang, B. Yang, Z.J. Li, X.T. Qin, Q.H. Zhang, L.C. Lei, M. Qiu, G. Wu, Y. Hou, highly active ruthenium sites stabilized by modulating electron-feeding for sustainable acidic oxygen-evolution electrocatalysis, Energy Environ. Sci. 15 (2022) 2356–2365.

[63]C. Hu, L. Zhang, J. Gong, Recent progress made in the mechanism comprehension and design of electrocatalysts for alkaline water splitting, Energy Environ. Sci., 12 (9) (2019) 2620-2645

[64] C. Wang, R. Wang, Y. Peng, J. Chen, J. Li, Iron tungsten mixed composite as a robust oxygen evolution electrocatalyst, Chem. Commun. 55 (2019) 10944–10947.

[65] F. Luo, R. Xu, S. Ma, Q. Zhang, H. Hu, K. Qu, S. Xiao, Z. Yang, W. Cai, Engineering oxygen vacancies of cobalt tungstate nanoparticles enable efficient water splitting in alkaline medium, Appl. Catal. B Environ. 259 (2019) 118090. https://doi.org/10.1016/j.apcatb.2019.118090.

[66] S. Kumaravel, P. Thiruvengetam, S.R. Ede, K. Karthick, S. Anantharaj, S. Sam Sankar, S. Kundu, Cobalt tungsten oxide hydroxide hydrate (CTOHH) on DNA scaffold: An excellent bi-functional catalyst for oxygen evolution reaction (OER) and aromatic alcohol oxidation, Dalt. Trans. 48 (2019) 17117–17131.

[67] G. Karkera, T. Sarkar, D. Bharadwaj, Design and Development of Efficient Bifunctional Catalysts by Tuning the Electronic Properties of Cobalt – Manganese Tungstate for Oxygen Reduction and Evolution Reactions, Chem Cat Chem. 9 (2017) 3681 –3690.

[68] R. Karthik, P.M. Sha, S. Chen, R. Sukanya, G. Dhakal, J. Shim, Investigation on microstructural impacts to electrochemical performances of strontium tungstate as efficient bifunctional catalyst for hydrogen and oxygen evolution reactions, J. Taiwan Inst. Chem. Eng. 126 (2021) 145–153.

[69] W. Shao, Y. Xia, X. Luo, L. Bai, J. Zhang, G. Sun, C. Xie, Structurally distorted wolframite-type Co x Fe 1-x WO 4 solid solution for enhanced oxygen evolution reaction, Nano Energy. 50 (2018) 717–722.

[70] M. Nakayama, A. Takeda, H. Maruyama, V. Kumbhar, O. Crosnier, Cobalt-substituted iron-based wolframite synthesized via polyol route for efficient oxygen evolution reaction, Electrochem. Commun.120 (2020) 106834.

[71] K. Selvakumar, T.H. Oh, Y. Wang, A.M. Prasanna, M. Arunpandian, T. Sadhasivam, P. Sami, M. Swaminathan, Rational design of single tungsten/cobalt atom oxide anchored on the TiO2-rGO: A highly efficient electrocatalyst for water splitting and photocatalyst for decomposition of pharmaceutical pollutant, Sep. Purif. Technol. 303 (2022) 122298.